Propagation and stability of waves of electrical activity in the cerebral cortex

P. A. Robinson,[1,*] C. J. Rennie,[1,2,†] and J. J. Wright[3,‡]
[1]*School of Physics, University of Sydney, New South Wales 2006, Australia*
[2]*Department of Medical Physics and Cognitive Neuroscience Unit, Westmead Hospital, Westmead, New South Wales 2145, Australia*
[3]*Mental Health Research Institute, Parkville, Victoria 3052, Australia*
(Received 23 December 1996)

Nonlinear equations are introduced to model the behavior of the waves of cortical electrical activity that are responsible for signals observed in electroencephalography. These equations incorporate nonlinearities, axonal and dendritic lags, excitatory and inhibitory neuronal populations, and the two-dimensional nature of the cortex, while rendering nonlinear features far more tractable than previous formulations, both analytically and numerically. The model equations are first used to calculate steady-state levels of cortical activity for various levels of stimulation. Dispersion equations for linear waves are then derived analytically and an analytic expression is found for the linear stability boundary beyond which a seizure will occur. The effects of boundary conditions in determining global eigenmodes are also studied in various geometries and the corresponding eigenfrequencies are found. Numerical results confirm the analytic ones, which are also found to reproduce existing results in the relevant limits, thereby elucidating the limits of validity of previous approximations. [S1063-651X(97)06006-6]

PACS number(s): 87.22.Jb, 87.22.As, 87.10+e

I. INTRODUCTION

Measurement of electrical activity in the cerebral cortex by means of electrodes on the scalp or the cortical surface is a commonly used tool in neuroscience and medicine. Detailed multichannel recordings of activity resulting from neuronal firings are routinely made, showing complex spatial and temporal patterns in the cortical regions where cognitive tasks are performed. These signals, known as electroencephalograms or EEGs, display sufficient consistency that their coarse morphological and spectral features may be empirically identified and quantified. The frequency content of EEG and variations in the power spectrum with cognitive state have been well characterized [1], velocities of EEG waves have been estimated [2], and typical features of the EEG response to external stimuli (so-called *event related potentials*) have been measured. Unfortunately, the connection between recorded EEGs and the underlying neuronal dynamics (and *a fortiori* cognition) remains poorly understood. A few of the most basic properties of cortical waves appear to be established [3], but virtually everything beyond this level is the subject of considerable debate and the wealth of experimental data is largely wasted in the absence of a more solid theoretical framework within which to analyze it.

Numerous models of cortical activity have been developed at a variety of levels of description. At the most fundamental level are neural networks, which attempt to describe the interconnections between individual neurons with varying degrees of idealization [4]. We term such simulations *microscopic* because of their incorporation of microstructure and neglect of long-range interconnections. Most notably, Freeman has modeled the EEG arising from the olfactory bulb of animals, during the perception of odors, by uniting estimates of physiological parameters within a system of nonlinear equations [5]. However, other methods are called for when models for microscopic, highly nonlinear neuronal events are extended to the large scale required to describe the macroscopic EEG waves of the cerebral cortex. Because of the huge numbers of neurons ($\sim 10^{10}$) in the cortex, smoothed-parameter models have been introduced to study global properties of cortical activity. Such models implicitly treat the cortex as a continuum (although they may be discretized for computation), characterized by mean densities of interconnections between neurons (which occur at *synapses*), mean neuronal firing rates, etc., with means taken over volumes large enough to include many neurons. Theoretical justifications for this ''mass action'' approximation have been given by Stevens [6] and Wright and Liley [7] and the resulting match with experimental findings has been discussed by several authors [7].

Both microscopic and continuum models typically include both *excitatory* and *inhibitory* inputs to a given neuron, which may itself be either excitatory or inhibitory in its action on other neurons. Excitatory inputs tend to increase the firing rate of a given neuron, while inhibitory ones reduce it, with both effects being nonlinear due, for example, to saturation at a maximum physiologically possible firing rate. Thus, in general, continuum models must incorporate mean densities of both populations of neurons, and of both types of interconnections, as well as the two neuronal firing rates. Delays in the propagation of signals through neurons (which are highly elongated) must also be included. These delays are of two types: *dendritic* lags, in which incoming signals are delayed in the dendritic fibers (see Fig. 1), and *axonal* delays of outgoing signals due to the finite propagation velocity along the axon.

The first continuum model [9,10] included excitatory and inhibitory populations in an infinite, linearized, one-dimensional (1D) model. With suitable adjustment of parameters, this model was able to reproduce the characteristic ~ 10 Hz frequency of the alpha rhythm, but omitted nonlin-

*Electronic address: robinson@physics.usyd.edu.au
†Electronic address: rennie@physics.usyd.edu.au
‡Electronic address: jjw@cortex.mhri.edu.au

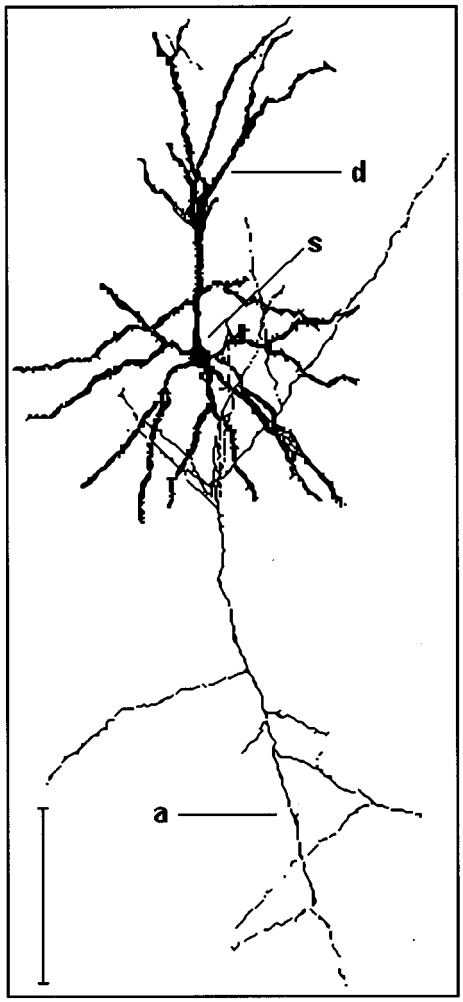

FIG. 1. A typical neuron of the cerebral cortex, from a Golgi stain (Ref. [8]). The scale bar represents 0.1 mm. Pulsed signals are generated at the soma (s) and propagate over the axonal tree (a) to make contact, at synaptic junctions, with the dendritic trees (d) of thousands of other neurons. Synaptic inputs are summed by the dendrites, and axonal pulses generated if the soma is depolarized beyond the cell's threshold.

ear effects, axonal delays, and the convolutions of the cortex.

Nunez [11,12] added axonal delays in order to investigate global modes. This model permitted wave solutions and, with the imposition of boundary conditions, the excitation of global eigenmodes. Nunez solved this model analytically for a 1D loop cortex, and for two-dimensional cortexes with periodic and with spheroidal boundary conditions (i.e., ignoring the more complicated convoluted form of the real cortex, and the inhomogeneity of cortical connections), interpreting observed cortical wave frequencies in terms of discrete eigenfrequencies. This model predicted global modes whose frequencies approximately match those of the major cerebral rhythms. In particular, the alpha rhythm was interpreted as being at the fundamental cortical eigenfrequency.

Wright and Liley [13–15] introduced a spatially discretized model in which the cortex is treated as 2D and divided into patches, each of which is parametrized by the mean densities of excitatory and inhibitory neurons, their mean firing rates, and their mean densities of interconnections (i.e., of synapses). Nonlinear effects and axonal and dendritic delays were all included, with a Green-function formulation describing the interconnections between patches as a function of their spatial and temporal separation. This model incorporated all relevant effects mentioned above, except convolutions and nonuniformities in cortical connectivity, while allowing for the imposition of a variety of boundary conditions. Moreover, its parameters were largely physiologically measurable, a significant advantage when comparing its predictions with measurements. However, simulations based on it have been limited to very small systems (or very coarse resolution in larger systems) due to its formulation in terms of Green functions, which are very slow to evaluate, and a numerically intensive treatment of dendritic lags.

The central purpose of this paper is to introduce a model of cortical electrical activity which includes nonlinearities, axonal and dendritic time lags, variable geometries and boundary conditions in 2D, and which permits analytic studies of wave properties and stability, while speeding computation to the point that whole-cortex simulations are possible with good resolution. This is accomplished in Sec. II by introducing a continuum wave-equation model to replace the linear parts of Wright and Liley's [13–15] discrete Green-function one, and also by simplifying their treatment of dendritic lags. The new model is not identical to that of Wright and Liley, but incorporates the same underlying neurophysics to a similar degree of approximation. Neither model addresses the question of filtering of cortical signals through the skull to determine the scalp EEG, a problem that can be avoided in any case by using magnetoencephalograms (MEGs) based on the magnetic signals associated with neural activity. The task of the remainder of the paper is to lay the mathematical basis for analysis of this model and obtain its basic properties. In Secs. III and IV we investigate the steady-state properties of the model and study the propagation and stability of small perturbations in the limit of an infinite medium. Periodic and spherical boundary conditions are imposed in Sec. V to investigate the properties of global eigenmodes and the eigenfrequencies are calculated for typical human parameters. An algorithm for numerical study of our model is described in Sec. VI and its output is used to verify key analytic results obtained in earlier sections.

II. CORTICAL MODEL

In this section we describe the relevant neurophysics and neurophysiology and incorporate it into a continuum model of cortical activity. The relationships of this model to those of Wright and Liley [13–15] and Nunez [11,12] are described in this section and Sec. IV, respectively.

A. Model equations

An excitatory neuron such as the one shown in Fig. 1 emits pulses (i.e., fires) at a mean rate q_e that is determined by the potentials generated in the dendritic tree by the synaptic inputs of thousands of other neurons. Threshold potentials, above which high firing rates occur, are not identical for all neurons, but have a centrally peaked distribution. We can then make a continuum approximation by replacing q_e with a local mean value Q_e, averaged over many neurons,

and introduce the mean dendritic potential V_e. Similar considerations apply for inhibitory neurons, denoted by the subscript i. Taking account of the spread of individual threshold potentials, one then finds the nonlinear relationship

$$Q_{e,i}=\frac{1}{1+e^{-C(V_{e,i}-V_0)}}, \tag{1}$$

$$\frac{dQ_{e,i}}{dV_{e,i}}=\frac{Ce^{-C(V_{e,i}-V_0)}}{[1+e^{-C(V_{e,i}-V_0)}]^2} \tag{2}$$

$$=CQ_{e,i}(1-Q_{e,i}), \tag{3}$$

where C is a positive constant and we have assumed the distribution (2) of threshold potentials relative to the mean value V_0 [a Gaussian distribution would be equally compatible with physiological measurements, yielding an error function in place of Eq. (1)]. In Eqs. (1) and (2), Q_e is measured in units of the maximum value possible (250–1000 s^{-1} per neuron), and potentials are measured in units of the characteristic standard deviation of the threshold distribution. Suitable values of the constants in Eqs. (1) and (2) are $C=1.82$ and $V_0=3$ [14].

Within a particular neuron, the relationship between the rate of arrival of incoming pulses, Q_{ae} or Q_{ai}, and the corresponding potential, V_e or V_i, is complicated. The induced transmembrane voltage perturbation propagates along the dendrites in a way that depends on the local dendritic capacitance and resistivity [5]. However, for the situation considered here of aggregate neural masses, we adopt the empirical finding that the temporal spread and conduction delay within an individual neuron's dendritic tree may be described by a simple impulse response. Specifically, Freeman [5] found that one can write

$$V_{e,i}(\mathbf{r},t)=g\int_{-\infty}^{t}w(t-t')Q_{ae,ai}(\mathbf{r},t')dt', \tag{4}$$

where $w(u)$ is a non-negative weight function, with a characteristic width of ≈ 10 ms and

$$\int_0^\infty w(u)du=1. \tag{5}$$

A suitable choice for $w(u)$ is

$$w(u)=\begin{cases}\dfrac{\alpha\beta}{\beta-\alpha}(e^{-\alpha u}-e^{-\beta u}), & \beta\neq\alpha \quad (6)\\ \alpha^2 u e^{-\alpha u}, & \alpha=\beta \quad (7)\end{cases}$$

for $u>0$, where α and β are positive constants. This function, shown in Fig. 2, peaks at $u_p=\ln(\beta/\alpha)/(\beta-\alpha)$ for $\alpha\neq\beta$ and at $u_p=1/\alpha$ for $\alpha=\beta$. This peak location can be chosen to be approximately 5 ms to correspond reasonably closely to physiological parameters [5,9,10], although some authors favor somewhat larger values with $\alpha\approx\beta\approx 400$ s^{-1} [16].

In general, Eq. (4) is a convolution that is difficult to handle analytically or numerically. However, the choice of

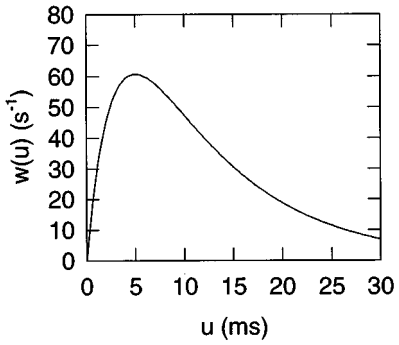

FIG. 2. Weight function $w(u)$ given by Eq. (6) for $\alpha=100$ s^{-1} and $\beta=350$ s^{-1}.

Eq. (6) enables Eq. (4) to be split into two ordinary differential equations via the introduction of auxiliary potentials $U_{e,i}$ and $W_{e,i}$, with

$$U_{e,i}(\mathbf{r},t)=\int_{-\infty}^{t}e^{-\alpha(t-t')}Q_{ae,ai}(\mathbf{r},t')dt', \tag{8}$$

$$W_{e,i}(\mathbf{r},t)=\int_{-\infty}^{t}e^{-\beta(t-t')}Q_{ae,ai}(\mathbf{r},t')dt', \tag{9}$$

$$V_{e,i}(\mathbf{r},t)=g\frac{\alpha\beta}{\beta-\alpha}[U_{e,i}(\mathbf{r},t)-W_{e,i}(\mathbf{r},t)]. \tag{10}$$

We find

$$\frac{dU_{e,i}(\mathbf{r},t)}{dt}=Q_{ae,ai}(\mathbf{r},t)-\alpha U_{e,i}(\mathbf{r},t), \tag{11}$$

$$\frac{dW_{e,i}(\mathbf{r},t)}{dt}=Q_{ae,ai}(\mathbf{r},t)-\beta W_{e,i}(\mathbf{r},t) \tag{12}$$

for $\beta\neq\alpha$. For $\alpha=\beta$, one can work directly with $V_{e,i}$ using the equation

$$\left(\frac{d^2}{dt^2}+2\alpha\frac{d}{dt}+\alpha^2\right)V_{e,i}(\mathbf{r},t)=g\alpha^2Q_{ae,ai}(\mathbf{r},t). \tag{13}$$

Equations (11) and (12), or Eq. (13), are much simpler to treat than the general case (4), but preserve all the essential physics. For applications in which only the characteristic time scale of the response $w(u)$ is important, one may assume $\beta\gg\alpha\approx 100$ s^{-1} and omit W.

When a neuron fires, the pulses propagate along the axon and axonal tree to provide incoming pulses at other neurons various distances away. The strength of interaction decreases as the number of synapses decreases with increasing distance. If we assume a characteristic axonal propagation velocity v and an isotropic distribution of axons in the continuum approximation, we can approximate the outward propagation of pulse density as a wave $\phi_{e,i}$ generated by the source $Q_{e,i}$. We thus find

$$\left(\frac{\partial^2}{\partial t^2}+2\gamma_{e,i}\frac{\partial}{\partial t}+\gamma_{e,i}^2-v^2\nabla^2\right)\phi_{e,i}(\mathbf{r},t)=\gamma_{e,i}^2 Q_{e,i}(\mathbf{r},t), \tag{14}$$

where $\gamma_{e,i}=v/r_{e,i}$ and $r_{e,i}$ is the characteristic range of the axons (assumed to have an approximately exponentially decreasing distribution at large ranges). Appendix A discusses the connection between Eq. (14) and the axonal range distribution and explores generalizations of this equation to anisotropic media and media in which there is more than one characteristic axonal range. Typical values of the constants in Eq. (14) are $r_e=0.08$ m and $r_i\approx 10^{-4}$ m for humans.

The incoming potentials Q_{ae} and Q_{ai} at a particular location comprise contributions from the wave potentials $\phi_{e,i}$ and inputs external to the cortex. These inputs are usually split into two classes: a uniform mean *nonspecific* excitation $Q_{\rm ns}$ resulting from the sum total of inputs from noncortical structures in the brain aside from those involved in a particular stimulus under study, and a *specific* excitation Q_s due to stimuli, which is defined here to include both noisy and coherent components which may or may not be spatially localized (e.g., in the visual cortex in response to a visual stimulus). The resulting equations are

$$Q_{ae}(\mathbf{r},t)=M_e Q_s(\mathbf{r},t)+\mu_e Q_{\rm ns}+a_{ee}\phi_e(\mathbf{r},t)-a_{ei}\phi_i(\mathbf{r},t), \tag{15}$$

$$Q_{ai}(\mathbf{r},t)=M_i Q_s(\mathbf{r},t)+\mu_i Q_{\rm ns}+a_{ie}\phi_e(\mathbf{r},t)-a_{ii}\phi_i(\mathbf{r},t). \tag{16}$$

The constants M_e and M_i determine the strength of coupling of specific inputs to excitatory neurons and inhibitory ones, respectively. Likewise, μ_e and μ_i represent the densities of synapses associated with nonspecific stimuli. The parameters a_{ee}, a_{ei}, a_{ie}, and a_{ii} are the synaptic densities associated with excitatory and inhibitory inputs to excitatory and inhibitory neurons. Note that we have defined $Q_{\rm ns}$ to be constant in time and space, while Q_s may vary in time and space but is defined here to have zero spatial and temporal means.

If the range of the inhibitory axons is sufficiently short, their inhibition can be considered to be a local effect and axonal delays can be neglected. In this case, every inhibitory pulse is immediately received locally and one can replace ϕ_i by Q_i in Eqs. (15) and (16) and omit the inhibitory version of Eq. (14). This *local inhibition* approximation limits the validity of the resulting equations to scales $\gg r_i\approx$ 0.1 mm, which is not problematical in practice because the finest-scale probes currently applied to the cortical surface are arrays with separation of order 1 mm [10], while scalp electrodes typically have separations of 20–50 mm. Naturally, if one wishes to explore possible long-range inhibitory interactions, this approximation can be easily relaxed.

Our model is characterized by the system of seven equations (1), (10)–(12), and (14)–(16). Typical values of the constants in these equations are given in Table I for the cortexes of mouse, cat, and human. Also quoted are values for the equivalent radius R_0 of a spherical cortex with the same area as the actual convoluted one, and the linear size L_0 of a square cortex with the same property. The quantities M_e and M_i have not been measured.

TABLE I. Estimated typical values for mouse, cat, and human of the parameters defined in the text. Most are taken from Refs. [15,16].

Parameter	Mouse	Cat	Human
a_{ee}	0.8023	0.844	0.853
a_{ii}	0.0112	0.004	0.002
a_{ie}	0.1186	0.122	0.126
a_{ei}	0.0626	0.022	0.011
μ_e	0.0046	0.007	0.007
μ_i	0.0007	0.001	0.001
r_e(mm)	2	2.7	84
v (m s^{-1})	9	9	9
R_0 (mm)	3.8	5.1	157
L_0 (mm)	13	18	558
g	25	37	36

B. Comparison with Wright and Liley's model

Wright and Liley [7,13–15] developed a model similar to the present one. Its similarities and differences are discussed here. A similar discussion for Nunez's linear model [11,12] is given in Sec. IV A.

The first point of similarity between the two models is that both use the form (1) for the relationship between $Q_{e,i}$ and $V_{e,i}$. Equation (4) is also the same in both models, but the present choice for $w(t)$ enables the convenient forms (10)–(13) to be obtained. In contrast, Wright and Liley [7,13–15] used a less physiologically justifiable triangular function to approximate the curve shown in Fig. 2, and evaluated the convolution (4) by direct integration. Numerically, this led to large demands on processing and storage (see Sec. VI).

The main difference between the two models is in the treatment of axonal propagation. Wright and Liley made the local approximation $\phi_i=Q_i$ (although they did not describe it in these terms) and employed a Green-function formulation in place of Eqs. (14)–(16). Their corresponding equations for Q_{ae} and Q_{ai} in terms of Q_e and Q_i were in discretized form and involved additional parameters describing the coupling of a given discrete region to itself. Discretization is an unnecessary complication here, so we give their equations in the following equivalent continuum form:

$$Q_{ae}(\mathbf{r},t)=M_e Q_s(\mathbf{r},t)+\mu_e Q_{\rm ns}-a_{ei}Q_i(\mathbf{r},t)+a_{ee}\int d^2\mathbf{r}'\int dt'\; G(\mathbf{r},t;\mathbf{r}',t')Q_e(\mathbf{r}',t'), \tag{17}$$

$$Q_{ai}(\mathbf{r},t)=M_i Q_s(\mathbf{r},t)+\mu_i Q_{\rm ns}-a_{ii}Q_i(\mathbf{r},t)+a_{ie}\int d^2\mathbf{r}'\int dt'\; G(\mathbf{r},t;\mathbf{r}',t')Q_e(\mathbf{r}',t'), \tag{18}$$

$$G(\mathbf{r},t;\mathbf{r}',t')=G(|\mathbf{r}-\mathbf{r}'|)\,\delta(t-t'-|\mathbf{r}-\mathbf{r}'|/v). \tag{19}$$

In these equations ϕ_e is expressed as an integral over the retarded Green function (19), which corresponds to signals

TABLE II. Relationship between symbols for quantities used here and those used by Wright and Liley in previous work. Note the reversal of the ordering of the mixed subscripts ei and ie in the present work relative to Wright and Liley's notation.

Symbol used here	Symbol used by Wright and Liley
a_{ee}	$\alpha_{ee}+\beta_{ee}$
a_{ii}	β_{ii}
a_{ie}	$\alpha_{ei}+\beta_{ei}$
a_{ei}	β_{ie}
μ_e	μ_{ee}
μ_i	μ_{ei}
M_e	M_{ee}
M_i	M_{ei}

that propagate at a velocity v. This integral is slow to compute numerically and involves a large amount of storage (see Sec. VI); to date these factors have limited simulations using Eqs. (17) and (18) to relatively small grids, which do not always provide adequate resolution for the desired applications. In addition, in their discrete form, they involved additional parameters associated with the scale of the discretization. One advantage is that the form of the spatial part of the Green function can be chosen at will, with Wright and Liley using a Gaussian to approximate the decreasing synaptic density at large $|\mathbf{r}-\mathbf{r}'|$. Appendix A contains a discussion of the relationship of this Green function to the one implicit in the present work.

The notation used in the present work is somewhat different from that used previously by Wright and Liley [7,13–15]. Changes have been made partly because some of their parameters are redundant in the present formulation, and partly to conform more closely with conventional usage in physics and mathematics. The relationships are given in Table II.

III. STEADY STATE

Understanding of the dynamics of our model begins by determining the uniform, steady-state behavior. Evaluating the integral in Eq. (4) for this special case and setting all derivatives to zero in Eqs. (14)–(16) yields

$$V_{e,i}=gQ_{ae,ai}, \tag{20}$$

$$\phi_{e,i}=Q_{e,i}, \tag{21}$$

$$Q_{ae}=\mu_e Q_{\rm ns}+a_{ee}\phi_e-a_{ei}\phi_i, \tag{22}$$

$$Q_{ai}=\mu_i Q_{\rm ns}+a_{ie}\phi_e-a_{ii}\phi_i, \tag{23}$$

where all quantities have spatially uniform steady-state values. Equation (21) can be used to eliminate $\phi_{e,i}$ from Eqs. (22) and (23). Then Eqs. (20), (22), and (23) are used to elimate $V_{e,i}$ from Eq. (1), in favor of $Q_{e,i}$. These steps yield

$$\exp[CV_0-gC(\mu_e Q_{\rm ns}+a_{ee}Q_e-a_{ei}Q_i)]=\frac{1}{Q_e}-1, \tag{24}$$

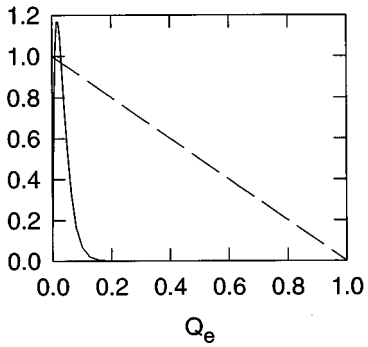

FIG. 3. Graphical solution of Eq. (26). The left and right sides of Eq. (26) are shown as the curve and straight line, respectively, for a particular case. There are three solutions if the peak of the curve lies above the straight line, as shown, but only one otherwise (located very near $Q_e=1$).

$$\exp[CV_0-gC(\mu_i Q_{\rm ns}+a_{ie}Q_e-a_{ii}Q_i)]=\frac{1}{Q_i}-1. \tag{25}$$

Equation (24) can be used to eliminate Q_i from Eq. (25) to give a single, rather cumbersome (but numerically straightforward), equation for the steady-state value of Q_e, whence the other steady-state quantities can be determined using Eqs. (20)–(24). Rather than treat this equation analytically here, we approximate Eqs. (24) and (25) and compare our results with numerical solutions of the exact equations.

Noting from Table I that physiological measurements imply $a_{ei}\ll a_{ee}$, Eq. (24) implies

$$Q_e\exp[CV_0-gC(\mu_e Q_{ns}+a_{ee}Q_e)]\approx 1-Q_e. \tag{26}$$

The left side of Eq. (26) is non-negative, with a single maximum where $gCa_{ee}Q_e=1$; at large Q_e it decreases exponentially fast. Figure 3 shows graphically that Eq. (26) can have either one solution or three, depending mainly on the values of V_0 and $Q_{\rm ns}$. One solution, always present, is located very close to $Q_e=1$, with

$$Q_e\approx 1-\exp[CV_0-gC(\mu_e Q_{\rm ns}+a_{ee}-a_{ei})], \tag{27}$$

$$Q_i\approx 1-\exp[CV_0-gC(\mu_i Q_{\rm ns}+a_{ie}-a_{ii})]. \tag{28}$$

The other two solutions, which only exist for small values of $Q_{\rm ns}$, are located at small values of Q_e. If we neglect Q_e on the right of Eq. (26), these solutions are

$$Q_e=(gCa_{ee})^{-1}\ln\{B^{-1}\ln[B^{-1}\ln(\cdots)]\}, \tag{29}$$

$$Q_e=(gCa_{ee})^{-1}B\,\exp\{B\exp[B\,\exp(\cdots)]\}, \tag{30}$$

$$B=gCa_{ee}\exp(gC\mu_e Q_{\rm ns}-CV_0). \tag{31}$$

When, for purposes of numerical evaluation, Eqs. (29) and (30) are recast in an iterative form, they become, respectively,

$$x_{n+1}=\ln(x_n/B), \tag{32}$$

$$x_{n+1}=B\,\exp(x_n), \tag{33}$$

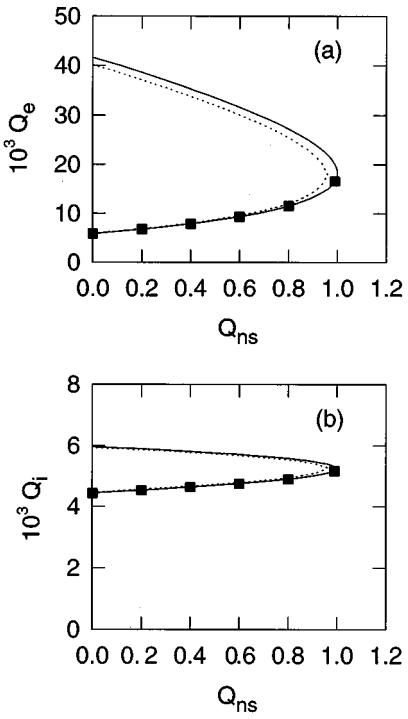

FIG. 4. Steady-state values vs $Q_{\rm ns}$ for the human parameters from Table I. The approximate solutions (29), (30), and (32) are shown as dashed curves, while exact solutions of Eqs. (24) and (25) are drawn solid. The square symbols show steady-state values obtained in the fully nonlinear simulations discussed in Sec. VI B. (a) Q_e. (b) Q_i.

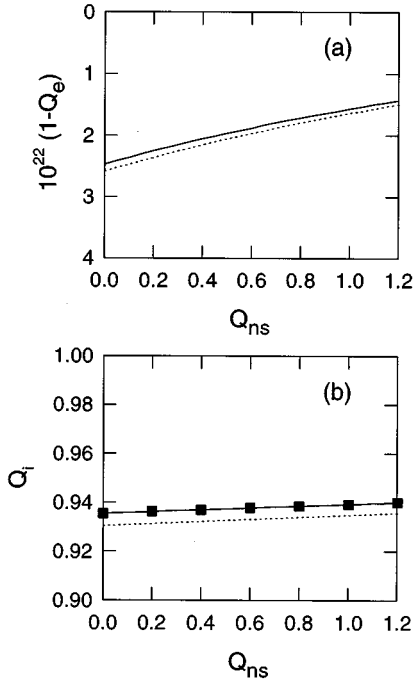

FIG. 5. Steady-state values vs $Q_{\rm ns}$ for the human parameters from Table I. The approximate solutions (27) and (28) are shown as dashed curves, while exact solutions of (24) and (25) are drawn solid. The square symbols show steady-state values of Q_i obtained in the fully nonlinear simulations described in Sec. VI B. (However, these simulations lacked sufficient precision to give useful steady-state values for $1-Q_e$.) (a) $1-Q_e$. (b) Q_i.

respectively, where in both cases Q_e is related to the limit x_∞ by

$$Q_e=(gCa_{ee})^{-1}x_\infty . \tag{34}$$

Equation (32) is found to converge to the larger of the two solutions, while Eq. (33) converges to the smaller solution. The corresponding values of Q_i are given by

$$Q_i=Q_e\exp[-gC(\mu_e-\mu_i)Q_{\rm ns}-gC(a_{ee}-a_{ie})Q_e]. \tag{35}$$

Note that when $B=e^{-1}$, then $Q_e=(gCa_{ee})^{-1}$ according to both Eqs. (29) and (30). The solutions (29) and (30) are only valid for $B\leqslant e^{-1}$, which places an upper bound on $Q_{\rm ns}$ in the low-Q_e steady state:

$$Q_{\rm ns}<[CV_0-1-\ln(gCa_{ee})]/(gC\mu_e). \tag{36}$$

For non-negative $Q_{\rm ns}$ this criterion also implies

$$g<\frac{e^{CV_0-1}}{Ca_{ee}}, \tag{37}$$

for low-Q_e steady-state solutions to exist. The solutions (27)–(35) can be substituted into Eqs. (20)–(23) to obtain steady-state values of other quantities.

Figure 4 compares the approximate solutions (29) and (30) with the numerical solution of Eqs. (24) and (25) for the human parameters from Table I. Figure 5 shows similar results for the fixed point given by Eqs. (27) and (28). In all cases the agreement is seen to be good. The approximation is least satisfactory near the rightmost point of the locus of solutions in Fig. 4. For example, Eq. (36) gives $Q_{\rm ns}<0.9520$ for the existence of low-Q_e solutions, whereas the full equations yield $Q_{\rm ns}<1.0000$. The small errors present in Eqs. (29)–(35), and demonstrated in Figs. 4 and 5, arise from the neglect of Q_e on the right side of Eq. (26). This neglect is justified on experimental grounds where it is found that in the normal cortex typical rates of less than 20 pulses per second per neuron are observed, compared with a maximum possible rate of 250–1000 s^{-1} [4,17]. The square symbols in Figs. 4 and 5 are discussed in Sec. VI B.

In summary, we have found three fixed points of Eqs. (24) and (25). One, given by Eq. (27), corresponds to a seizure in which all neurons are firing at near their maximum possible rate. The next two, given by Eqs. (29) and (30), involve low firing rates of all neurons, similar to what is seen in the normal state of the cortex. We discuss these steady states further in Sec. IV B, once their stability characteristics have been clarified.

IV. WAVE PROPERTIES: INFINITE MEDIUM

In this section we consider the properties of small perturbations about the fixed points found in Sec. III. This yields the dispersion relations and growth or damping rates of the waves, and the linear stability boundary of the system. We do not consider nonlinear wave propagation or instabilities.

A. Wave dispersion

To determine the linear wave properties of our model, we must first linearize Eq. (1), writing

$$Q_{e,i}=Q_{e,i}^{(0)}+\rho_{e,i}[V_{e,i}-V_{e,i}^{(0)}], \tag{38}$$

where $Q_{e,i}^{(0)}$ and $V_{e,i}^{(0)}$ are the relevant steady-state values from Sec. III and $\rho_{e,i}=dQ_{e,i}/dV_{e,i}$ at this point. Fourier transforming Eqs. (38) and (10)–(16), and deleting the components $(\mathbf{k},\omega)=(\mathbf{0},0)$ (which were treated in Sec. III) then yields

$$Q_{e,i}=\rho_{e,i}V_{e,i}, \tag{39}$$

$$V_{e,i}=gLQ_{ae,ai}, \tag{40}$$

$$L=\frac{\alpha\beta}{(\alpha-i\omega)(\beta-i\omega)}, \tag{41}$$

$$D_{e,i}\phi_{e,i}=\gamma_{e,i}^2Q_{e,i}, \tag{42}$$

$$D_{e,i}=(\gamma_{e,i}-i\omega)^2+k^2v^2, \tag{43}$$

$$Q_{ae}=M_eQ_s+a_{ee}\phi_e-a_{ei}\phi_i, \tag{44}$$

$$Q_{ai}=M_iQ_s+a_{ie}\phi_e-a_{ii}\phi_i, \tag{45}$$

where the arguments $\mathbf{k}$ and ω are implicit. It is worth noting from Eqs. (40) and (41) that $|L|$ decreases monotonically with ω and, hence, the dendrites act as low-pass filters that tend to remove frequencies $\omega>\min\{\alpha,\beta\}$.

We can write $Q_{e,i}$ in terms of $Q_{ae,ai}$ using Eqs. (39) and (40). Equations (44) and (45) can then be used to write $Q_{e,i}$ in terms of $\phi_{e,i}$. If the results are substituted into Eq. (43), we find

$$(D_e-F_ea_{ee})\phi_e+F_ea_{ei}\phi_i=F_eM_eQ_s, \tag{46}$$

$$(D_i+F_ia_{ii})\phi_i-F_ia_{ie}\phi_e=F_iM_iQ_s, \tag{47}$$

$$F_{e,i}=\gamma_{e,i}^2\rho_{e,i}gL. \tag{48}$$

A dispersion equation for ϕ_e alone results from elimination of ϕ_i from Eqs. (46) and (47). Instead of following this route, we make the local-inhibition approximation $\phi_i=Q_i$ based on the short range of the inhibitory fibers. As mentioned earlier, this approximation limits us to considering waves with wavelengths longer than a few tenths of a mm. We then find

$$(D_e-F_ea_{ee})\phi_e=F_e(M_eQ_s-a_{ei}Q_i). \tag{49}$$

Elimination of Q_i in favor of ϕ_e, as before, then yields

$$Q_i=\frac{F_i}{\gamma_i^2+F_ia_{ii}}(M_iQ_s+a_{ie}\phi_e). \tag{50}$$

After substitution of Eq. (50) into Eq. (49) we then find the wave equation

$$(D_e-F_ea_{ee})\phi_e=F_eM_eQ_s, \tag{51}$$

where some small terms have been neglected subject to the assumption that $M_i\gg M_e$ is *not* satisfied. The linear response of the cortex to a specific signal Q_s is given by Eq. (51) in Fourier space. One significant point is that all the inhibitory coefficients have disappeared, having been discarded as small quantities in going from Eqs. (49) and (50) to Eq. (51). Hence it is the excitatory component that determines the long-range behavior.

For freely propagating waves, Eq. (51) with $Q_s=0$ gives the dispersion equation

$$(\alpha-i\omega)(\beta-i\omega)D_e-\alpha\beta\gamma_e^2G=0. \tag{52}$$

The quantity G, given by

$$G=\rho_egga_{ee}, \tag{53}$$

is the net gain in the loop in which a low-frequency, low-k perturbation of magnitude ϵ in ϕ_e gives rise to perturbations $a_{ee}\epsilon$ in Q_{ae}, $ga_{ee}\epsilon$ in V_e, $\rho_ega_{ee}\epsilon$ in Q_e, and $\rho_ega_{ee}\epsilon=G\epsilon$ in ϕ_e. Equivalently, G is the mean number of pulses stimulated by each pulse emitted. Equation (52) can be approximated as

$$(\alpha-i\omega)D_e-\alpha\gamma_e^2G=0, \tag{54}$$

$$D_e-\gamma_e^2G=0, \tag{55}$$

for $\beta\gg\alpha,\omega$ and for $\beta,\alpha\gg\omega$, respectively. For typical physiological parameters [10,18] one has $\alpha=100\ \mathrm{s}^{-1}$ and $\beta=350\ \mathrm{s}^{-1}$, and the approximations (54) and (55) are applicable for frequencies $f=\omega/2\pi$ given by $f\ll 55$ Hz, and $f\ll 15$ Hz, respectively. Only the first of these is appropriate to study the full range of normally recognized human EEG rhythms, although Eq. (55) may be semiquantitatively useful. In the single-parameter case $\alpha=\beta\approx 200\ \mathrm{s}^{-1}$, Eq. (54) does not apply but Eq. (55) is valid provided $f\ll 30$ Hz.

Equations (52) and (54) incorporate dendritic lags to generalize the corresponding linear wave equation obtained by Nunez [11,12], which omitted these lags and was of the form (55). Nunez's equation applies in the limit in which these lags are negligible. However, the discussion in the preceding paragraph implies that this is at best semiquantitatively correct for the alpha rhythm ($f\approx 10$ Hz) and is an increasingly poor approximation at higher frequencies. Examples of the solutions of Eqs. (52)–(55) are given in Sec. IV C, after we have discussed the question of stability.

B. Linear stability

Equations (52), (54), and (55) are polynomials in $u=-i\omega$ with purely real coefficients. Hence solutions for u are either purely real or occur in complex-conjugate pairs. Growing solutions correspond to $\mathrm{Im}\ \omega=\mathrm{Re}\ u>0$. From Eq. (55) we find

$$\omega=-i\gamma_e\pm i(\gamma_e^2G-k^2v^2)^{1/2}. \tag{56}$$

This result immediately implies that an instability occurs for

$$G>1+k^2v^2/\gamma_e^2=1+k^2r_e^2, \tag{57}$$

with equality in Eq. (57) defining the instability boundary. The least stable perturbations are at $k=0$. At large k, the waves are damped, propagating modes, with $\omega \approx \pm kv - i\gamma_e$. In the case of the quartic equation (52) at large k, D_e can be either large or small. If it is large, we find two purely damped modes with $\omega \approx -i\alpha, -i\beta$. If it is large, there are two propagating modes that approach the high-k solutions of Eq. (56). Since there can be only four solutions to a quartic, these four modes are the only ones. Similar reasoning can also be applied to the cubic equation (54), yielding the same modes except for the one at $\omega \approx -i\beta$.

The quartic and cubic equations, (52) and (54), can be solved analytically in the general case, but the solutions are too unwieldy to be useful. Here we obtain the stability boundary for these equations by considering the special case where the root(s) with the largest Re u are marginally stable with Re $u=0$. The stability boundary for the cubic equation can be obtained from that of the quartic in the limit $\beta \to \infty$, so we consider only Eq. (52) here.

There are two ways in which instability can first set in and from which the instability boundary can be calculated: either a real root can reach the point $u=0$ or a pair of complex-conjugate roots can reach the point where they are purely imaginary. The latter case breaks into two subcases in which the other two roots have negative real parts and are either purely real or are complex conjugates. In the case of a real root being the first to reach the instability boundary, the boundary corresponds to $u=0$. Equation (52) immediately yields the criterion (57) for instability. The dendritic parameters α and β do not enter this criterion because the frequency is zero at the point of marginal stability, whence $L=1$ in Eq. (41). In Appendix B we demonstrate that the cases in which a pair of complex-conjugate roots are the first to become unstable have no consistent solution for $G>0$. Hence Eq. (57) is the instability criterion for Eqs. (52), (54), and (55) in all circumstances.

For $k=0$, the criterion (57) can be used to determine the stability of the fixed points found in Sec. III. Using Eqs. (3) and (53), we find stability only for

$$Q_e(1-Q_e) < (gCa_{ee})^{-1}. \tag{58}$$

This criterion immediately implies that the high-Q_e root (27) is stable. By imposing the same approximation used in deriving (27), (29), and (30), namely that $Q_e \ll 1$, Eq. (58) becomes $Q_e < (gCa_{ee})^{-1}$. As noted above, this value of Q_e is the one at which the solutions (29) and (30) coincide, and is located at the rightmost point in Fig. 4(a). Consequently, this inequality identifies the *lower* of the two solutions, Eq. (30), as being stable, while Eq. (29) is unstable. Thus there are two basins of attraction in a linear approximation, corresponding to the two stable roots.

(i) A ''normal'' low-activity state, corresponding to Eq. (30), in which all neurons fire at rates far below their physiological limits. This state corresponds to the stable one found previously in numerical calculations [7,13–15] and to normal levels of cortical activity in nature.

(ii) A saturated high-activity state, corresponding to Eq. (27), where physiologically maximal firing rates are approached during a seizure. This state was also seen previously in numerical work [7,14] and presumably corresponds to a grand mal seizure in nature.

Numerical calculations show empirically that nonlinear systems initialized with Q_e below the upper of the two low-Q_e solutions tend to converge to the lower one, while systems initialized with higher Q_e converge to the solution (27). Thus Eq. (29) approximately defines the boundary between the basins of attraction even in the nonlinear case.

It has been remarked previously on many occasions that self-organizing systems such as the brain must by their very nature operate ''on the border of instability'' or ''on the edge of chaos'' [19]. Otherwise, complex behavior would not be possible because the system would either be unstable or would settle into a relatively quiescent state (or, at least, one of low complexity). We can measure the nearness of the cortex to marginal stability by taking the ratio of the damping rate at $k=0$ in Eq. (57) to the corresponding rate for $G=0$, since it is the cortical gain parameter G that controls stability. The resulting parameter $1-G^{1/2}$ is approximately 0.4 for the normal state of the mouse, cat, and human for the parameters in Table I, even for $Q_{ns}=0$. Thus, even without stimulation, the cortex is more than halfway to instability for the parameter values adopted here. In the more typical case in which $Q_{\rm ns}$ is sufficiently large that $Q_e=0.015$, the stability parameter is only 0.07, implying that the cortex is very near to instability under typical conditions.

C. Numerical solutions of dispersion relations

The dispersion relations (52), (54), and (55) are straightforward to solve numerically. Several sample solutions are examined in this section to illustrate the main features of stable and unstable waves, and the similarities and differences between the waves predicted by the three equations.

Figure 6 shows the real and imaginary parts of ω for the various modes predicted by Eqs. (52), (54), and (55), which predict four, three, and two modes, respectively. For the parameters given in the caption, the system is predicted to be stable for all k and, indeed, Im $\omega<0$ throughout. The solutions labeled ± 1 have $\omega \approx -i\gamma_e \pm kv$ at high k, in accord with the discussion in Sec. IV B. For these solutions, the group velocity $\mathbf{v}_g = \partial \mathrm{Re}\omega / \partial \mathbf{k}$ approaches $\pm v$ as k increases, implying that axonal propagation chiefly determines the propagation of electrocortical waves in this limit. This derived velocity is in accord with cortical and scalp measurements [2,20,21]. The solutions labeled $0L$ and $0H$ have $\omega \approx -i\alpha$ and $\omega \approx -i\beta$, respectively, at large k, also in accord with Sec. IV B. The three least damped modes are very similar in both the quartic and cubic cases, implying that the cubic approximation (54) is adequate under these circumstances. Important differences between the quadratic case and the other two are that the least damped mode is one of the pair ± 1 in the former case, and the $0L$ mode in the other, and that the quadratic case has no propagating modes for $k^2v^2 < \gamma_e^2 G$, in agreement with Eq. (56). Interestingly, the ± 1 and $0H$ solutions become less damped at high k, while the $0L$ solution becomes more heavily damped.

Figure 7 shows a case where the parameters correspond to an unstable solution to the steady-state equations at $k=0$. The mode structure is the same as in Fig. 6, except that there are growing solutions where Eq. (57) is satisfied. This

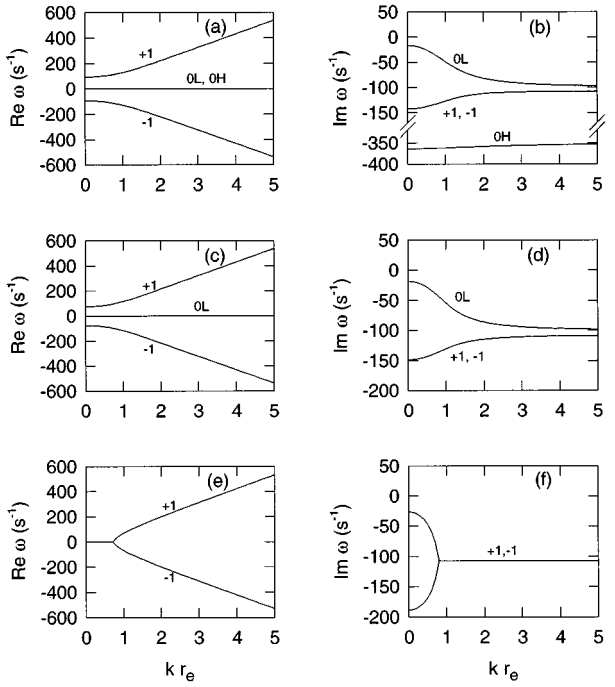

FIG. 6. Dispersion of the modes predicted by Eqs. (52), (54), and (55). The left column shows Reω, while the right shows Imω. The four roots predicted by Eq. (52) are shown in the top row of the figure, the three roots predicted by Eq. (54) are shown in the middle row, and the two roots predicted by Eq. (55) are shown in the bottom row. The parameters of the system are the human parameters from Table I with $G=0.57$, corresponding to the stable fixed point at $Q_{\rm ns}=0.7$. Propagating modes have either positive or negative Reω and are labeled $+1$ and -1. The two nonpropagating modes are labeled OL and OH as they are distinguished only by their degree of damping, which, reflecting the values of α and β, may be low or high. (a) Reω, quartic dispersion relation. (b) Imω, quartic dispersion relation. (c) Reω, cubic dispersion relation. (d) Imω, cubic dispersion relation. (e) Reω, quadratic dispersion relation. (f) Imω, quadratic dispersion relation.

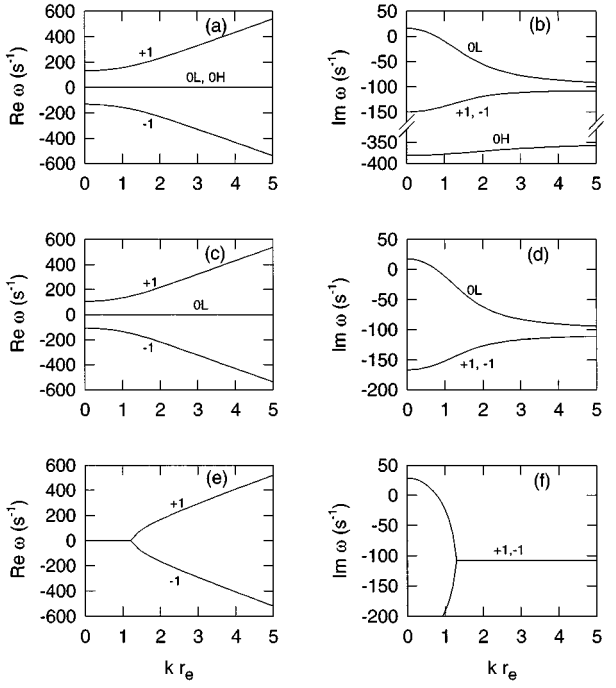

FIG. 7. Dispersion of the modes predicted by Eqs. (52), (54), and (55). The left column shows Reω, while the right shows Imω. The four roots predicted by Eq. (52) are shown in the top row of the figure, the three roots predicted by (54) are shown in the middle row, and the 2 roots predicted by Eq. (55) are shown in the bottom row. The parameters of the system are the human parameters from Table I with $G=1.602$, corresponding to the unstable fixed point at $Q_{\rm ns}=0.7$. Modes are labeled as in Fig. 6. (a) Reω, quartic dispersion relation. (b) Imω, quartic dispersion relation. (c) Reω, cubic dispersion relation. (d) Imω, cubic dispersion relation. (e) Reω, quadratic dispersion relation. (f) Imω, quadratic dispersion relation.

boundary is the same for quadratic, cubic, and quartic equations, as the discussion in Appendix B implies. The unstable wave is in the ± 1 branches in the quadratic case, and in the $0L$ branch in the other two cases. This anomaly in the quadratic case is due to the two solutions of Eq. (55) being the only ones available, which forces them to change their character from propagating to nonpropagating as k decreases, whereas higher-degree dispersion relations have a different topology.

V. WAVE PROPERTIES: FINITE MEDIUM

The previous two sections have explored the properties of our model for an infinite medium. Since the cortex is finite we now examine the effects of imposing boundary conditions on our equations. Two cases are considered here: periodic boundary conditions on a square cortex (i.e., a toroidal topology, but not geometry), and a spherical cortex. We do not consider the effects of cortical convolutions or inhomogeneities in this paper, except to choose the size of our square or sphere so its area equals that of the actual, convoluted cortex seen in nature. Both convolutions (or other reductions in symmetry) and inhomogeneities will lead to splitting of degenerate eigenfrequencies found below, a point noted by Nunez in the context of his linearized analysis [11,12].

A. Cortex with periodic boundary conditions

If we impose periodic boundary conditions on a rectangular cortex with edges of length L_x and L_y (both of which we will denote by L_0 when they are equal), the wave vector $\mathbf{k}$ is restricted to values $(2\pi n_x/L_x, 2\pi n_y/L_y)$ where n_x and n_y are integers. This corresponds to selecting out a series of discrete eigenmodes from dispersion curves such as those in Figs. 6 and 7 as having the only combinations of ω and k allowed in the finite cortex. Note that modes with equal and opposite values of n_x and/or n_y are always degenerate.

One important point to note is that, for $1<G<1+(2\pi r_e/\max\{L_x,L_y\})^2$, only the $k=0$ mode is unstable. Since $2\pi r_e \gtrsim L_0$ for the parameters in Table I, this can be a substantial range of parameter space. Thus, when considering the global linear stability of the brain, the problem can often be reduced to that of a single mode by virtue of the discrete nature of the eigenspectrum.

Table III lists Reω and Imω for solutions of Eq. (52) with human parameters from Table I, $G=0.57$, and periodic

TABLE III. Lowest eigenfrequencies for periodic boundary conditions on a square cortex for the human parameters from Table I. In addition, $\alpha=100\ \mathrm{s}^{-1}$, $\beta=350\ \mathrm{s}^{-1}$, $Q_{\mathrm{ns}}=0.7$, and $G=\rho_e g a_{ee}=0.57$. The real and imaginary parts of ω are given as a function of the quantum numbers n_x and n_y for modes that have positive real frequency, in order of increasing real frequency. Purely damped, nonpropagating modes are omitted. Only cases with $n_y \geqslant n_x \geqslant 0$ are listed because the modes are degenerate under each of the replacements $n_x \rightarrow -n_x$, $n_y \rightarrow -n_y$, and $n_x \leftrightarrow n_y$.

n_x	n_y	k (m^{-1})	Reω	Imω
0	0	0.0	93.1	−142.7
0	1	11.3	124.4	−128.7
1	1	15.9	155.6	−120.3
0	2	22.5	208.8	−113.4
1	2	25.2	231.4	−111.9
2	2	31.8	289.5	−109.8
0	3	33.8	306.6	−109.4
1	3	35.6	322.7	−109.1
2	3	40.6	367.1	−108.6
0	4	45.0	406.6	−108.3
1	4	46.4	419.0	−108.2
3	3	47.8	431.1	−108.1

boundary conditions for small n_x and n_y in order of increasing Reω. Purely damped, nonpropagating modes are not listed. The tabulated values all lie on the branch labeled $+1$ in Figs. 6(a) and 6(b); the parameters of the branch labeled -1 are obtained by reversing the sign of Reω. Three important points to note are that (i) the imaginary part of ω gives the characteristic width of each mode in frequency; since these widths are larger than the separation between modes for the parameters of Table III, one would not expect to see well defined resonances when these modes are excited by white noise, for example, (ii) the prominence of the resonances is reduced when, as in the present situation, the scale length of the damping, r_e, is less that the circumference of the system, and (iii) the minimum frequency of a propagating mode is ~ 15 Hz, which lies in the typical physiological range.

B. Spherical cortex

If we Fourier transform Eq. (52) in space, we find the form

$$v^2\nabla^2\phi_e(\mathbf{r})=[(\gamma_e-i\omega)^2-L\gamma_e^2G]\phi_e(\mathbf{r}), \tag{59}$$

where the temporal variation $\sim\exp(-i\omega t)$ has been separated off. If we consider the spatial component of any wave equation on a spherical cortex, the eigenfunctions satisfy

$$-\nabla^2\phi_e=\frac{l(l+1)}{R_0^2}\phi_e, \tag{60}$$

where l is the principal quantum number of the eigenfunction in question, and R_0 is the radius of the sphere. Solutions are of the form $\phi_e=e^{im\varphi}P_l^m(\cos\theta)$ where P_l^m is an associated Legendre function [22], m is the azimuthal quantum number, and θ and φ are standard spherical coordinates. As a result of this constraint, Eq. (59) leads to a dispersion relation very like Eq. (52) except that the quantity k^2 is replaced by $l(l+1)/R_0^2$. The azimuthal quantum number m does not appear in the dispersion relation, so all $2l+1$ modes for fixed l are degenerate for a precisely spherical cortex.

TABLE IV. Lowest eigenfrequencies for periodic boundary conditions on a spherical cortex for the human parameters from Table I with $Q_{\mathrm{ns}}=0.7$, $\alpha=100\ \mathrm{s}^{-1}$, $\beta=350\ \mathrm{s}^{-1}$, and $G=0.57$. The real and imaginary parts of ω are given as a function of the quantum number l for modes that have positive real frequency. Purely damped, nonpropagating modes are omitted. The eigenfrequencies are independent of the quantum number m.

l	Reω (s^{-1})	Imω (s^{-1})
0	93.1	−142.7
1	113.0	−133.2
2	153.2	−120.8
3	204.9	−113.8
4	260.1	−110.6
5	316.3	−109.2
6	373.1	−108.5

Table IV lists Reω and Imω for solutions of Eq. (52) with human parameters from Table I, $G=0.57$, and spherical boundary conditions. Values for small l are given in order of increasing Reω and purely damped, nonpropagating modes are not listed. The eigenfrequencies increase approximately as $\sqrt{l(l+1)}$ at large l and are in the range observed for cortical frequencies. As in the periodic cortex, the mode widths exceed their separations, so we do not expect noise to excite clear resonances for these parameters.

VI. NUMERICAL RESULTS

In order to study the dynamics of our full nonlinear model, Eqs (1), (10)–(12), and (14)–(16) have been implemented numerically. This section outlines the methods used and numerical confirmations of the key analytic results obtained in earlier sections.

A. Methods

Of our seven equations, implementation of Eqs. (1), (10), (15), and (16) is trivial, since they involve no derivatives. Likewise, Eqs. (11) and (12) present no difficulties because they are ordinary differential equations in t.

In solving the wave equation (14), we make the local-inhibition approximation $\phi_i=Q_i$, which removes the need to follow ϕ_i via a wave equation, but restricts us to wavelengths $\gg 0.1$ mm as discussed in Sec. II A. Initially, we implement Eq. (14) on a square grid with periodic boundary conditions, corresponding to a cortex with toroidal topology. By introducing the auxiliary field $\psi=e^{-\gamma_e t}\phi_e$, Eq. (14) is transformed to the form of the standard wave equation:

$$\left[\frac{\partial^2}{\partial t^2}-v^2\nabla^2\right]\psi(\mathbf{r},t)=\gamma_e^2e^{-\gamma_e t}Q_e(\mathbf{r},t). \tag{61}$$

This enables us to use standard routines to step ψ forward in time, although we actually store ϕ_e at each step to avoid

underflow at large t due to the exponential factor in Eq. (61). We solve Eq. (61) in coordinate space, rather than Fourier space, so as to enable the most straightforward generalization to more complicated geometries in future, where Fourier methods are not applicable (e.g., on a convoluted cortex). Our approach will also allow inhomogeneities and anisotropies to be relatively easily incorporated in future.

On an $N\times N$ grid, the runtime of our code scales as N^2 per time step. This represents a major improvement on the Green-function method used in previous nonlinear calculations [7,13–15], where the runtime required to evaluate the Green functions scaled as N^4 per time step. Direct comparisons of the two methods verify a speedup of order N^2, which enables us to attain adequate whole-cortex resolution. Storage is also dramatically reduced through the use of Eqs. (10)–(12) and (14), which are time local and require storage of only a few configurations of the system needed by the time-stepping routines (storage $\sim N^2$). In contrast, previous methods stored of order 100 previous configurations of the system to treat the dendritic lags (storage $\sim 100N^2$) and of order N previous configurations to evaluate the Green function (storage $\sim N^3$).

B. Steady-state solutions

In Sec. III approximate steady-state solutions were derived, and in Figs. 4 and 5 a comparison was made with the exact solutions for Q_e and Q_i. With the numerical implementation of the dynamical equations, as described above, it is possible to determine the accuracy of the analytic approximations made previously and of the resulting fixed-point estimates. This was done for several different values of $Q_{\rm ns}$, including values for which there are three possible fixed points, and larger values of $Q_{\rm ns}$ for which there is just one fixed point. We chose the grid ratio to be $p=v\Delta t/\Delta x=0.1$. A grid of 100×100 was employed, although the results are not sensitive to grid size. There is an important dependence on initial conditions though. The stable states both have their own basins of attraction characterized by low and by high firing rates, and so we set $Q_e=Q_i=0$ initially for one series of simulations, and $Q_e=Q_i=1$ for another. The other variables were initialized according to Eqs. (20)–(23). The results are shown as square symbols in Figs. 4 and 5 (showing low and high firing-rate steady-state solutions, respectively). As expected, the former set of simulations converged to the stable, lowest firing-rate fixed point, except for $Q_{\rm ns}\geqslant 1.000$, in which case no such solution exists and they converged to the stable, high firing-rate fixed point. The latter series, with Q_e and Q_i initialized to unity, always converged to the high firing-rate fixed point.

From the discussion of linear stability in Sec. IV B, we expect the upper branch of the curves in Fig. 4 to be unstable. This expectation was supported by a further set of simulations in which $Q_{\rm ns}$ was arbitarily set to 0.6 and Q_e was initialized to values in the range 0.000–0.050 at intervals of 0.005, to cover the range defined by the two low-Q_e steady-state solutions for $Q_{\rm ns}=0.6$, namely, $Q_e=0.009$ and $Q_e=0.032$. For completeness, initial values $Q_e=0.100$–1.000 at intervals of 0.100 were also used. With Q_i initialized to zero, it was found that simulations having Q_e initialized to 0.000–0.030 converged to the lowest of the steady-state solutions, and the remainder to the $Q_e\simeq 1$ solution. With Q_i initialized to unity, almost the same result was obtained: simulations having Q_e initialized to 0.000–0.035 converged to the lowest of the steady-state solutions, and the remainder to the $Q_e\simeq 1$ solution.

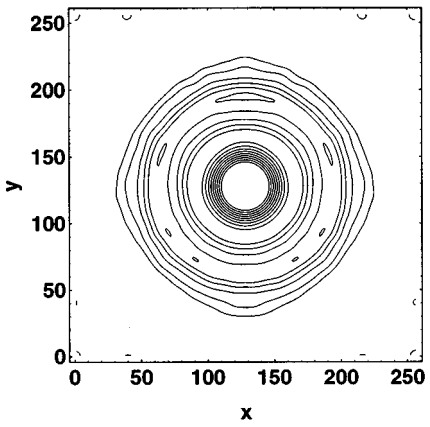

FIG. 8. The distribution of Q_e at one time in a simulation on a 256×256 grid. The system was driven by a 500 s^{-1} sinusoidal signal Q_s applied to a 6×6 central area. $\Delta x=\Delta y=2.18$ mm and $\Delta t=0.05$ ms. In the figure x and y are measured in units of Δx and Δy, respectively.

This series of simulations supports our theoretical linear-stability result that the upper branch of solutions in Fig. 4 is unstable, because convergence is only ever to the other two solutions. Indeed, initializing all variables as nearly as possible to those of an upper branch fixed point resulted in unstable behavior: after initial slow evolution, it eventually converged to one of the other two fixed points.

In addition to the above, we can infer the approximate form of the basin of attraction of the stable solutions. Altering the initialization of Q_i from zero to unity had only a small effect on the ultimate steady state. Whether the initial value of Q_e is larger or smaller than its value at the unstable fixed point is therefore the principal determinant of ultimate state of the system; the initial value of Q_i can affect that choice only when Q_e is close to that of the unstable fixed point.

With regard to the reproducibility of the fixed points using the full nonlinear simulation, errors in the final values of Q_e and Q_i were of the order of 10^{-5} for $p=v\Delta t/\Delta x=0.1$. The accuracy of simulations worsens for larger values of p, and when $p\geqslant 1/\sqrt{2}$ (related to the Courant condition for the two-dimensional explicit difference method) the numerical solutions become unstable. Much smaller values of p lead to cumulative rounding errors unless more sophisticated time-stepping routines are used. The choice of p also affects the accuracy of convergence, as do the initial values of the variables. Variation of the initial value of Q_e gave rise to marginally different values of the final steady-state variables. These differences, also of order 10^{-5}, provide another estimate of the accuracy of the calculations. Of course such small errors are negligible in applications because cerebral parameters are known only approximately and measurements cannot distinguish such small differences in firing rates.

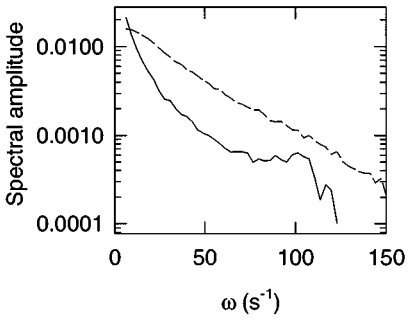

FIG. 9. Spectral amplitudes for the case of periodic boundary conditions. A grid of 20×20 points was used, with $\Delta x=\Delta y=27.9$ mm, driven by spatially coherent white noise Q_s along the column defined by $x=0$, and the resulting activity Q_e measured at a point $x=10\Delta x$, $y=10\Delta y$ for a total of 100×2.048 s. Spectral amplitudes are normalized to the spectrum of the input signal. $Q_{\rm ns}=0.7$, $\alpha=100\ {\rm s}^{-1}$, and $\beta=350\ {\rm s}^{-1}$. The dashed line is for $r_e=0.15L_0$, $\gamma_e=108\ {\rm s}^{-1}$, and the solid line is for $r_e=1.50L_0$, $\gamma_e=10.8\ {\rm s}^{-1}$. All other parameters were as in Table III.

C. Wave propagation

The existence of roots of the dispersion relation having nonzero real parts means that the system supports traveling waves. This is demonstrated in Fig. 8, in which a 256×256 grid has its central 6×6 points driven by a sinusoidal signal with $\omega=500\ {\rm s}^{-1}$. The amplitude of the driving signal was 0.01 and $Q_{\rm ns}$ was set to 0.7. With reference to Fig. 4(a), this was sufficient to maintain activities (a) within the basin of attraction of the nonseizure state, and (b) within physiological limits. A concentric distribution of traveling waves is evident, and the scale length of damping ($r_e=83.7$ mm $=40$ grid units) may be appreciated. This degree of damping does not allow accurate estimation of the wavelength, but the expectation, from the dispersion relation (52), of $\lambda=52$ grid units is at least approximately borne out.

D. Power spectra

As another demonstration of the dynamical properties of the model, we consider the square cortex with periodic boundary conditions discussed in Sec. V A, and in Table III. Figure 9 is the result of driving this system along one column ($x=0$, $y=0-19\Delta y$, $\Delta y=27.9$ mm) with spatially uniform white noise, and recording the values of Q_e at a site distant from the sites of stimulation. A total of 100 periods of 2.048 s were recorded, transformed to give amplitude spectra, and averaged. The nonspecific excitation $Q_{\rm ns}$ was set equal to 0.7 to make this figure match the eigenfrequencies listed in Table III. With all other system parameters as in Table I (human) the dashed line in Fig. 9 was obtained. This shows no apparent resonance because for the eigenfrequencies to be clearly visible the damping length r_e must be $\gtrsim L_0$. To demonstrate resonance, r_e was set to the somewhat unrealistic figure of $1.5L_0$, and a resonance peak was then obtained (Fig. 9, solid line). The location of the peak is also consistent with the dispersion relation (52): with this revised value of r_e, the $n_x=n_y=0$ mode becomes purely damped and the first oscillatory mode is then the $n_x=1,n_y=0$ (or $n_x=0,n_y=1$) mode having an expected frequency of 101 $\rm s^{-1}$. (The next mode is at 143 $\rm s^{-1}$, but there is so little signal at frequencies $\gtrsim120\ {\rm s}^{-1}$ as to be beyond the precision of the analysis.)

A further point demonstrated by this example is the relationship between damping and the width of the resonance peak. Increasing r_e had the effect of reducing $\gamma_e=v/r_e$ to $10.8\ {\rm s}^{-1}$, and this is reflected in the observed resonance peak width.

The main implications of this example are (i) very low values of $\gamma_e=v/r_e$ are needed to see resonances, as discussed in Sec. V A, and (ii) experimentally Imω can be estimated from the width of the alpha resonance. The first point sheds some doubt on Nunez's global resonance picture, unless γ_e is smaller than previously thought.

VII. SUMMARY AND DISCUSSION

Motivated by the need for a formulation of cerebral activity that is analytically and numerically tractable, we have formulated a set of nonlinear continuum equations that satisfies these requirements. These equations embody the nonlinear response (on average) of neurons to imposed potentials, the presence of excitatory and inhibitory populations, and axonal and dendritic lags, and provide the framework for a wide variety of analytic and numerical calculations.

Analytically, we have used our model to study the steady-state behavior of the cortex, and its stability, as well as linear waves propagating in bounded and unbounded models of the cortex. Numerically, the speed at which our nonlinear system can be simulated is of the same order as that for the corresponding linear one, thereby enabling adequate whole-brain resolution to be obtained in a 2D nonlinear model. The main results of the present study are summarized next.

(i) Dendritic lags have been treated in a way that is both simpler and closer to physiological measurements than in previous work. This enables analytic treatment and reduces numerical runtime and storage requirements.

(ii) The propagation of axonal signals, including axonal delays, has been formulated in terms of a wave equation. This bears some similarities to previous wave equations, but does not assume that the system as a whole is linear. Our wave-equation formulation is analytically tractable and dramatically faster to treat numerically than its Green-function predecessor. Numerical storage requirements are also far lower.

(iii) The results emphasize the importance of both dendritic and axonal delays in determining the dispersion relations of cortical waves and, hence, global eigenfunctions.

(iv) The criteria for ignoring the finite range of inhibitory fibers have been made more explicit.

(v) An analytic fixed-point analysis has been done to determine the steady states of the system. Three fixed points have been found, one of which is unstable. Of the other two, one represents a ''normal'' state of low activity, while the other represents a saturated ''seizure'' state in which activity is near its maximum.

(vi) Dispersion equations have been derived for small-amplitude linear waves. These equations incorporate both axonal propagation and dendritic lags. The limit in which dendritic lags can be neglected is elucidated and it is shown that an earlier equation [12] is reproduced in this limit.

(vii) A stability boundary has been described, beyond which a seizure will set in. Under normal conditions the cortex is not far from this boundary, consistent with the view that complex, self-organizing systems must be near ''the edge of stability'' to function properly. This emphasizes the prospect for future work to analyze internal controls of cerebral dynamics, such as regulation of local and global inhibition, which may exploit this near-marginally stable behavior to produce much richer dynamics [7].

(viii) The effects of boundary conditions have been studied for a square cortex with periodic boundary conditions and for a spherical cortex, yielding discrete eigenfrequencies in the relevant physiological ranges.

(ix) Numerical solutions of our model equations have confirmed the existence of one steady-state solution with a high firing rate, and two steady-state solutions with a low firing rate. Of the latter pair, only the lower is stable, and both require $Q_{\rm ns}$ to be less than a limiting value given approximately by Eq. (36). If $Q_{\rm ns}$ is large enough the system will saturate. The system will also saturate if the state is moved to some point with Q_e greater than that of the unstable fixed point.

(x) Numerical simulations have demonstrated the existence of traveling waves.

(xi) Numerical simulations have confirmed theoretical results that sharp resonances are impossible unless the damping parameter γ_e is substantially smaller than previously supposed. This casts some doubt on previous suggestions that the alpha rhythm is a global resonance of the cortex. If, however, this rhythm *is* a global resonance, the imaginary part of its frequency can be estimated experimentally from its width.

ACKNOWLEDGMENTS

Two of the authors (P.A.R. and C.J.R.) thank the Mental Health Research Institute of Victoria and the University of Iowa for their hospitality during visits in which some of this work was undertaken. This work was supported by the Ross Trust, Melbourne.

APPENDIX A: GREEN FUNCTIONS AND GENERALIZED WAVE EQUATIONS

This appendix discusses the connection between the wave equation (14), its Green function, and the corresponding axonal range distribution. It then compares the Green function with that used by Wright and Liley [13,14], and explains how Eq. (14) can be generalized to a broader class of media.

1. Green functions

The solution of Eq. (14) can be written in terms of a Green function G as

$$\phi(\mathbf{r},t)=\int d^2\mathbf{r}'\int dt'\; G(\mathbf{r},t;\mathbf{r}',t')Q(\mathbf{r}',t'), \quad \text{(A1)}$$

where subscripts have been omitted for simplicity. In an isotropic medium, G depends only on the distance $R=|\mathbf{r}-\mathbf{r}'|$ and the time difference $\tau=t-t'$. The Fourier transform of the Green function can be immediately evaluated from the Fourier transforms of Eqs. (14) and (A1), giving

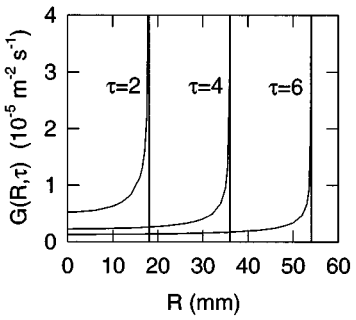

FIG. 10. Green function (A6) for $\gamma_e=108\ \mathrm{s}^{-1}$, $r_e=84$ mm, and $v=9\ \mathrm{m\ s}^{-1}$ for $t=2$, 4, and 6 ms, from left to right.

$$G(\mathbf{k},\omega)=\frac{\gamma^2}{(\gamma-i\omega)^2+k^2v^2}. \quad \text{(A2)}$$

The inverse Fourier transform of Eq. (A2) then yields

$$G(R,\tau)=\int\frac{d^2\mathbf{k}}{(2\pi)^2}\int\frac{d\omega}{2\pi}e^{i\mathbf{k}\cdot\mathbf{R}-i\omega\tau}G(\mathbf{k},\omega) \quad \text{(A3)}$$

$$=\frac{\gamma^2e^{-\gamma\tau}}{4\pi^2v}\int_0^\infty dk\ \sin(kv\tau)\int_0^{2\pi}d\theta\ e^{ikR\cos\theta} \quad \text{(A4)}$$

$$=\frac{\gamma^2e^{-\gamma\tau}}{2\pi v}\int_0^\infty dk\ \sin(kv\tau)J_0(kR) \quad \text{(A5)}$$

$$=\frac{\gamma^2e^{-\gamma\tau}}{2\pi v}\frac{1}{\sqrt{v^2\tau^2-R^2}}\Theta(v\tau-R), \quad \text{(A6)}$$

where polar coordinates, R and θ, are used to do the integral over $\mathbf{k}$, Θ is a unit step function, and only the retarded part of the propagator has been retained to avoid unphysical solutions that propagate backward in time. Note that

$$\int d^2\mathbf{R}\int d\tau\ G(R,\tau)=\int d^2\mathbf{R}\,\frac{\gamma^2}{2\pi v^2}K_0(R\gamma/v) \quad \text{(A7)}$$

$$=1, \quad \text{(A8)}$$

where K_0 is a modified Bessel function of the second kind (a Macdonald function) [22]. The result (A8) is required on physical grounds to ensure conservation of pulses. Note that the integrand in Eq. (A7) represents the time-integrated response at a distance R; i.e., the total number of pulses reaching a unit area at that distance.

Figure 10 shows Eq. (A6) at various times. One point to note is that $G(R,\tau)$ is not a δ function at $R=v\tau$, unlike in the better known three-dimensional case. Rather, it is a function that is concentrated close to the point $R=v\tau$, but with a tail at smaller R. Such behavior is also seen in the standard 2D wave equation without damping terms and is characteristic of wave propagation in a 2D geometry. Writing $G(R)=\int d\tau\ G(R,\tau)$, Eq. (A6) implies $G(R)=K_0(R/r_0)/2\pi r_0^2\sim(R/r_0)^{-1/2}\exp(-R/r_0)$ at large R, where $r_0=v/\gamma$, im-

plying that axons have a characteristic range r_0. At small R, $G(R)\sim-\ln(R/r_0)$, which may appear at first sight to be pathological. However, the total number of synapses at range R is proportional to $2\pi RG(R)$, which remains finite. Also, it should be remembered that this logarithmic singularity is present intrinsically in the standard 2D wave equation, which does not yield singular responses to nonsingular inputs. If desired, the singularity can be removed by replacing $K_0(r/r_0)$ by

$$r_0^{-2}K_0(R/r_0)-r_1^{-2}K_0(R/r_1), \tag{A9}$$

with $r_1\ll r_0$. This Green function has no singularity and corresponds to a pair of fields with characteristic ranges r_0 and r_1, and ϕ equal to their difference. In general, the second field requires the introduction of an additional wave equation but a local approximation may be possible since it has a short range.

A Green function of the form (A6) is implicit in the work of Nunez [12], who used a wave equation of the form (14) to study linear cortical waves. Wright and Liley's, form [7,13,14] involves a δ function, as in Eqs. (17) and (18), so the correspondence with the present work is not exact. Comparison of their distribution of axonal ranges with the present form is achieved by integrating over time, as in Eq. (A7). The result should be compared with Wright and Liley's $G(R)$. They typically chose $G(R)\propto\exp(-R^2/r_0^2)$, where r_0 is a constant; however, the closest large-R correspondence between the two models would be obtained by substituting the form (A7) for $G(R)$ in Wright and Liley's model.

2. Generalized wave equations

It is straightforward to generalize the wave equation (14) in a number of ways. Most obviously, one could replace it by the form

$$\left[\frac{\partial^2}{\partial t^2}+2\gamma\frac{\partial}{\partial t}+\gamma^2-v_1^2(\mathbf{e}_1\cdot\nabla)^2-v_2^2(\mathbf{e}_2\cdot\nabla)^2\right]\phi=\gamma^2Q, \tag{A10}$$

where the subscripts and arguments of ϕ and Q have again been omitted for simplicity. This equation represents a case of anisotropic propagation velocity, with velocities v_1 and v_2 along orthogonal principal axes $\mathbf{e}_1$ and $\mathbf{e}_2$. The effective axonal ranges in these two directions are then v_1/γ and v_2/γ.

A second way in which Eq. (14) can be generalized is to assume that there are a number of different axonal populations j characterized by different ranges r_{0j} and velocities v_j. This is an extension of the procedure described in the preceding section for removing the singularity in $G(R)$. In this more general case, one can write

$$\phi=\sum_j\phi_j, \tag{A11}$$

with an equation of the form (14) or (A10) for each j. This is also a suitable way to allow for a range of different propagation velocities, also parametrized by j [12]. Furthermore, it is straightforward to generalize Eq. (A10) by making the coefficients slowly varying functions of time and position.

APPENDIX B: INSTABILITY BOUNDARY ANALYSIS

In this appendix we outline the proof that the stability boundary for the quartic dispersion relation (52) cannot be set by a pair of complex-conjugate roots having $\mathrm{Re}u=0$, where $u=-i\omega$. In our proof by contradiction, we assume that there are two conjugate roots $u_1=iz$ and $u_2=-iz$ at the point of marginal stability, with $z>0$. We then show that this assumption contradicts the requirement $G\geqslant 0$, with G given by Eq. (53). Hence the stability boundary is set by the condition $u=0$, which leads to Eq. (56).

Equation (52) can be expanded to yield

$$\begin{aligned}0=&u^4+u^3(\alpha+\beta+2\gamma)+u^2[\alpha\beta+2\gamma(\alpha+\beta)+\gamma^2+k^2v^2]\\&+u[2\alpha\beta\gamma+(\alpha+\beta)(\gamma^2+k^2v^2)]\\&+\alpha\beta[\gamma^2(1-G)+k^2v^2],\end{aligned} \tag{B1}$$

where the subscript on γ_e has been omitted for simplicity.

1. Stable roots in a complex-conjugate pair

If we suppose that, at the point of marginal stability, there are two stable roots given by $u_3=-x+iy$ and $u_4=-x-iy$, where $x,y>0$, then

$$0=u^4+2xu^3+u^2(x^2+y^2+z^2)+2xz^2u+z^2(x^2+y^2). \tag{B2}$$

Equating the coefficients in Eqs. (B1) and (B2) and eliminating x and y yields

$$z^2=\frac{2\alpha\beta\gamma+(\alpha+\beta)(\gamma^2+k^2v^2)}{\alpha+\beta+2\gamma}, \tag{B3}$$

$$G=1+\frac{k^2v^2}{\gamma^2}-\frac{z^2}{\alpha\beta\gamma^2}[\alpha\beta+2\gamma(\alpha+\beta)+\gamma^2+k^2v^2-z^2]. \tag{B4}$$

Direct expansion of the right side of Eq. (B4), using Eq. (B3), shows that it is always negative for $x,y,z>0$, contradicting the required sign of G.

2. Stable roots real

The only remaining case is the one in which the two stable roots are real with values $u_3=-x$ and $u_4=-y$, for positive x and y. If we expand the resulting equation and equate coefficients with those in Eq. (B1) we again arrive at Eqs. (B3) and (B4). Hence this case also yields a contradiction, implying that Eq. (53) is the instability criterion under all circumstances.

[1] D.O. Walter, B.S. Kado, J.M. Rhodes, and W.R. Adey, Aerosp. Med. **38**, 371 (1967).

[2] F.H. Lopes da Silva and W. Storm van Leeuwin, in *Architectonics of the Cerebral Cortex*, edited by M.A. Brazier and H. Petsche (Raven, New York, 1978).

[3] M.H.J. Munk, P.R. Roelfsema, P. Konig, A.K. Engel, and W.

Singer, Science **272**, 271 (1996).
[4] D.J. Amit, *Modelling of Attractor Neural Networks* (Cambridge University Press, Cambridge, England, 1989).
[5] W.J. Freeman, in *Induced Rhythms of the Brain*, edited by E. Başar and T.H. Bullock (Birkhauser, Basel, 1991).
[6] C.F. Stevens, in *Large Scale Neuronal Theories of the Brain*, edited by C. Koch and J.L. Davies (MIT Press, Cambridge, MA, 1994).
[7] J.J. Wright and D.T.J. Liley, Behav. Brain Sci. **19**, 285 (1996).
[8] V. Braitenberg, in *Cortical Architectonics: General and Areal*, edited by M. Brazier and H. Petsche (Raven, New York, 1978).
[9] F.H. Lopes da Silva, A. Hoeks, A. Smits, and L.H. Zetterberg, Kybernetik **15**, 27 (1974).
[10] A. van Rotterdam, F.H. Lopes da Silva, J. van den Ende, M.A. Viergever, and A.J. Hermans, Bull. Meth. Biol. **44**, 283 (1982).
[11] P.L. Nunez, IEEE Trans. Biomed. Eng. **BME-21**, 473 (1974).
[12] P.L. Nunez, in *Neocortical Dynamics and Human EEG Rhythms*, edited by P.L. Nunez (Oxford, Oxford, 1995), Chaps. 9 and 11.
[13] J.J. Wright and D.T.J. Liley, Network: Comp. Neural Syst. **5**, 191 (1994).
[14] J.J. Wright and D.T.J. Liley, Biol. Cybern. **72**, 347 (1995).
[15] J.J. Wright, Biol. Cybern. (to be published).
[16] W. Rall, J. Neurophysiol. **30**, 1138 (1967).
[17] D.J. Amit and N. Brunel, Cereb. Cortex **7**, 237 (1997).
[18] W.J. Freeman, in *Handbook of Electroencephalography and Clinical Neurophysiology Vol. 1, Revised Series*, edited by A.S. Gevins and A. Rémond (Elsevier, Amsterdam, 1989).
[19] C. Langton, in *Artifical Life II*, edited by C. Langton, C. Taylor, J.D. Farmer, and S. Rassmussen (Addison-Wesley, Reading, MA, 1992).
[20] J.J. Wright and A.A. Sergejew, Electroencephalogr. Clin. Neurophysiol. **79**, 403 (1991).
[21] G. Burkitt, Ph.D. thesis, Swinburne University of Technology, Melbourne, 1994.
[22] *Handbook of Mathematical Functions*, edited by M. Abramowitz and I.A. Stegun (Dover, New York, 1970).